Multimodal Partial-Volume Correction: Application to ^{18}F-Fluoride PET/CT Bone Metastases Studies

Elisabetta Grecchi[1,2], Jim O'Doherty[3], Mattia Veronese[1], Charalampos Tsoumpas[2,4], Gary J. Cook[2,3], and Federico E. Turkheimer[1]

[1]Centre for Neuroimaging, Institute of Psychiatry, Psychology and Neuroscience King's College London, London, United Kingdom; [2]Division of Imaging Sciences & Biomedical Engineering, King's College London, London, United Kingdom; [3]PET Imaging Centre, Division of Imaging Sciences and Biomedical Engineering, King's College London, King's Health Partners, St. Thomas's Hospital, London, United Kingdom; and [4]Division of Biomedical Imaging, University of Leeds, Leeds, United Kingdom

[18]F-fluoride PET/CT offers the opportunity for accurate skeletal metastasis staging, compared with conventional imaging methods. ^{18}F-fluoride is a bone-specific tracer whose uptake depends on osteoblastic activity. Because of the resulting increase in bone mineralization and sclerosis, the osteoblastic process can also be detected morphologically in CT images. Although CT is characterized by high resolution, the potential of PET is limited by its lower spatial resolution and the resulting partial-volume effect. In this context, the synergy between PET and CT presents an opportunity to resolve this limitation using a novel multimodal approach called synergistic functional–structural resolution recovery (SFS-RR). Its performance is benchmarked against current resolution recovery technology using the point-spread function (PSF) of the scanner in the reconstruction procedure. **Methods:** The SFS-RR technique takes advantage of the multiresolution property of the wavelet transform applied to both functional and structural images to create a high-resolution PET image that exploits the structural information of CT. Although the method was originally conceived for PET/MR imaging of brain data, an ad hoc version for whole-body PET/CT is proposed here. Three phantom experiments and 2 datasets of metastatic bone ^{18}F-fluoride PET/CT images from primary prostate and breast cancer were used to test the algorithm performances. The SFS-RR images were compared with the manufacturer's PSF-based reconstruction using the standardized uptake value (SUV) and the metabolic volume as metrics for quantification. **Results:** When compared with standard PET images, the phantom experiments showed a bias reduction of 14% in activity and 1.3 cm^3 in volume estimates for PSF images and up to 20% and 2.5 cm^3 for the SFS-RR images. The SFS-RR images were characterized by a higher recovery coefficient (up to 60%) whereas noise levels remained comparable to those of standard PET. The clinical data showed an increase in the SUV estimates for SFS-RR images up to 34% for peak SUV and 50% for maximum SUV and mean SUV. Images were also characterized by sharper lesion contours and better lesion detectability. **Conclusion:** The proposed methodology generates PET images with improved quantitative and qualitative properties. Compared with standard methods, SFS-RR provides superior lesion segmentation and quantification, which may result in more accurate tumor characterization.

Up to 70% of patients with prostate and breast cancer will develop bone metastases (*1,2*). ^{18}F-fluoride has shown efficacy in both diagnosis and treatment response assessment (*3–6*), and recent studies on skeletal metastases report improved diagnostic sensitivity and specificity when morphologic evaluation from CT scans are combined with functional evaluation of ^{18}F-fluoride PET (*7,8*). This radiotracer accumulates at skeletal metastatic sites as a result of increased blood flow, osteoblastic activity, and bone mineralization (*9–11*). In prostate cancer, ^{18}F-fluoride accumulation corresponds to sites of osteosclerosis and increased bone density that are usually visible on CT (*12*).

Evaluation criteria for tumor staging and response assessment include visual or quantitative evaluation of the extent, intensity, and changes in ^{18}F-fluoride uptake in bone lesions (*13*). In this perspective, the influence of the partial-volume effect (PVE) is of importance (*14*) when comparing activity and morphologic changes before and after therapy (*15,16*) considering the poor image resolution and quantification bias resulting from activity spill-over. PVE in PET has been addressed with several image-based partial-volume correction (PVC) methods (*17*) that can be classified as either voxel-based methods, such as partition-based (*18*), multiresolution (*19,20*), or region-of-interest (ROI)–based techniques (*21,22*), which are limited by assumptions of radiotracer distribution homogeneity in the area of interest. A distinct approach consists of the incorporation of a model for the system point-spread function (PSF) within the image reconstruction algorithm to account for resolution degradation (*23,24*).

In this study, our aim was to correct for the PVE in whole-body ^{18}F-fluoride PET/CT to allow a more robust lesion classification in terms of activity quantification and volume definition. The methodology was developed from previous work by Shidahara et al. (*20*) and exploits the local functional–structural relationship of PET/CT in a synergistic fashion for a realistic noise-controlled resolution recovery of PET images, hence the name synergistic functional–structural resolution recovery (SFS-RR). Here, the SFS-RR algorithm is optimized for ^{18}F-fluoride PET given the correlation between functional
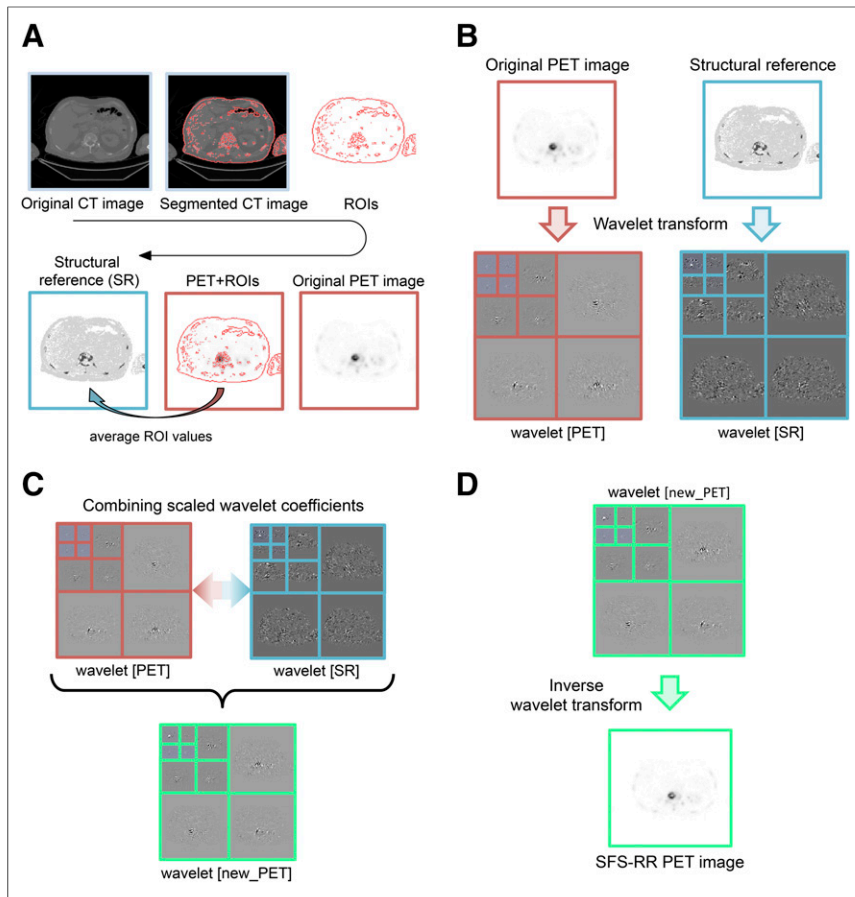
FIGURE 1. Graphical representation of SFS-RR algorithm. (A) Structural reference image required by SFS-RR algorithm is computed from CT and PET images. (B) Wavelet decomposition of functional and structural images. (C) Functional and structural wavelet coefficients are combined to get new high-resolution PET coefficients. (D) Inverse wavelet transform of coefficients obtained from step C resulting in the new high-resolution SFS-RR PET image. For detailed mathematic formulation, refer to supplemental materials.

(fluoride uptake) and morphologic (sclerosis) signals on PET and CT images. For benchmarking, the resulting images were compared with standard reconstructed PET images and images reconstructed with the inclusion of the PSF model (25).

MATERIALS AND METHODS

Image Resolution Recovery

The SFS-RR algorithm was first introduced by Shidahara et al. (20) for PVC of brain PET/MR data. The structural information was exploited by segmenting a T1-MR image through a probability atlas (26) defining 83 anatomic regions. Hence, the resolution recovery is ROI-based and relies on good coregistration between PET and MR images as well as between MR imaging and the probability atlas. The idea stems from previous concepts on wavelet-based resolution recovery (19) and denoising (27).

In this work, we developed SFS-RR further to fit a novel clinical requirement, specifically ^{18}F-fluoride PET/CT for detecting and monitoring bone metastases. The choice of the application is not fortuitous; in the first instance, PET/CT images provide synergistic information (i.e., both modalities show high image intensity in correspondence of lesions) and, second, they do not require additional coregistration as for 2 separate PET and MR acquisitions. Furthermore, all the structural information of interest is contained in the CT and can be automatically segmented for each subject with no need for a universal atlas.

The algorithm decomposes both functional (PET) and anatomic (CT) images into several resolution elements by means of a wavelet transform. The high-resolution components of both modalities are then combined together via a statistical model with appropriate scaling, resolution correction, and weighting, to create a high-resolution PET image that exploits the structural information, when present, but preserves PET data when matching structural data are not present.

Anatomic Image Segmentation

In their original work, Shidahara et al. (20) proposed the use of an anatomic brain atlas to obtain suitable anatomic images. In brain studies, this is a reasonable procedure given the possibility of normalizing to a common space (e.g., probabilistic atlas).

In whole-body PET/CT, the atlas-based approach is not feasible. In ^{18}F-fluoride PET/CT acquisitions, the good spatial correlation between morphologic and functional information is such that the CT images of each subject can be processed individually to highlight the structures of interest supplying the required structural base.

The first step consists of an initial coarse segmentation of the CT images based on thresholding the Hounsfield unit (HU) values as follows: bone ($100 \leq$ HU $< 1,400$), soft tissue ($0 \leq$ HU < 100), and fat ($-150 \leq$ HU < 0) (28).

Bone is further segmented into 100 bins after image histogram equalization. New intensity values are assigned to all the segmented regions. These intensity values are calculated from the average of each corresponding region in the original PET image to obtain the subject-specific structural reference image used as anatomic information for the SFS-RR algorithm (Supplemental Fig. 1; supplemental materials are available at http://jnm.snmjournals. org) (20,29).

Image segmentation and the SFS-RR algorithm implementation were both performed in Matlab R2011b (The MathWorks Inc.). The whole procedure is schematically described in Figure 1; for a more detailed mathematic exposition the reader is referred to the supplemental materials (Synergistic-Functional-Structural Resolution Recovery Algorithm section).

Phantom Data

For the evaluation of the SFS-RR method, we used the National Electrical Manufacturers Association International Electrotechnical Commission body phantom and an insert with 6 spheres of different volumes: 26.52 cm^3 (S1), 11.49 cm^3 (S2), 5.57 cm^3 (S3), 2.57 cm^3 (S4), 1.15 cm^3 (S5), and 0.52 cm^3 (S6). Compartments were filled with both iodinated contrast medium (CM) Omnipaque300 (GE Healthcare) (organic iodine [300 mg/mL]) and radioactive tracer ^{18}F-fluoride. We aimed to reproduce contrast levels between different structures in both the PET and the CT images as observed in clinical ^{18}F-fluoride bone scans. Specifically, we reproduced PET and CT contrasts as observed in normal soft tissue, normal bone, and metastatic bone. We performed 3 different experiments, changing the layout of CT and PET contrasts. This procedure aimed to account for

TABLE 1
CT Contrast Medium and PET Radiotracer Concentrations

Phantom compartments	Experiment 1		Experiment 2		Experiment 3		Sphere volume (mL)
	Iodine contrast medium (mg/mL)	^{18}F-FDG (kBq/mL)	Iodine contrast medium (mg/mL)	^{18}F-FDG (kBq/mL)	Iodine contrast medium (mg/mL)	^{18}F-FDG (kBq/mL)	
Background	1.08*	4.56*	1.20*	5.29*	1.20*	5.70*	9,700
S1	6.00†	53.20†	6.00†	66.50†	1.20*	5.70*	26.52
S2	6.00†	53.20†	42.00‡	187.00‡	41.20‡	227.00‡	11.49
S3	6.00†	53.20†	6.00†	66.50†	1.20*	5.70*	5.57
S4	1.00*	148.50‡	42.00‡	187.00‡	41.20‡	227.00‡	2.57
S5	1.00*	148.50‡	6.00†	66.50†	1.20*	5.70*	1.15
S6	1.00*	148.50‡	42.00‡	187.00‡	41.20‡	227.00‡	0.52

*Concentration resulting in image contrast comparable to normal soft tissue.
†Concentration resulting in image contrast comparable to normal bone.
‡Concentration resulting in image contrast comparable to metastatic bone.
Concentrations of iodine (from Omnipaque300) and ^{18}F-FDG injected in all phantom compartments for each experiment. Compartment volumes are also reported. Spheres 4–6, experiment 1, and spheres 1, 3, and 5, experiment 3, are filled with same radioactivity concentration as background; as a result they are indiscernible in PET image.

possible mismatches between functional and anatomic images (i.e., whereas a lesion would be detectable in only 1 imaging modality) resulting in a more robust method validation. A summary of CM and radiotracer concentrations used in each experiment is reported in Table 1. For a detailed description of the experimental procedure, we refer to Grecchi et al. (*30*).

Images were acquired on a Discovery 710 PET/CT scanner (GE Healthcare). CT scans were obtained with a routine clinical protocol (115 mA, 140 kVp, and 0.5-s gantry rotation speed) followed by a fully 3-dimensional PET time-of-flight acquisition. PET data were reconstructed using our routine clinical protocol, a standard time-of-flight ordered-subsets expectation maximization algorithm (24 subsets, 2 iterations) (Q.Core VuePoint FX [GE Healthcare], henceforth called standard PET). The resulting images were then processed with the SFS-RR algorithm. In addition, we reconstructed the same data with the inclusion of a PSF model into the standard time-of-flight ordered-subsets expectation maximization algorithm (Q.Core VuePoint FX-S [GE Healthcare], henceforth called PET-PSF).

All the images were finally smoothed with a gaussian 3-dimensional filter (full width at half maximum, 6.4 mm); this is required by PSF-reconstructed images as well when used in clinical routine given that increased noise levels hamper visual assessment.

Clinical Dataset

The impact of the proposed resolution recovery technique was tested with 2 different sets of oncologic patient data, both characterized by the presence of bone metastases. The institutional review board approved this study, and all subjects signed a written informed consent form.

The first dataset was a prospective observational study of patients with bone-predominant metastatic prostate cancer, at first diagnosis or at progression of disease, who were embarking on docetaxel chemotherapy. The second dataset was a prospective observational study of patients with bone-predominant metastatic breast cancer, at first diagnosis or at progression of disease, who were embarking on a new line of endocrine treatment in combination with bone-targeted therapy. In total, 7 patients
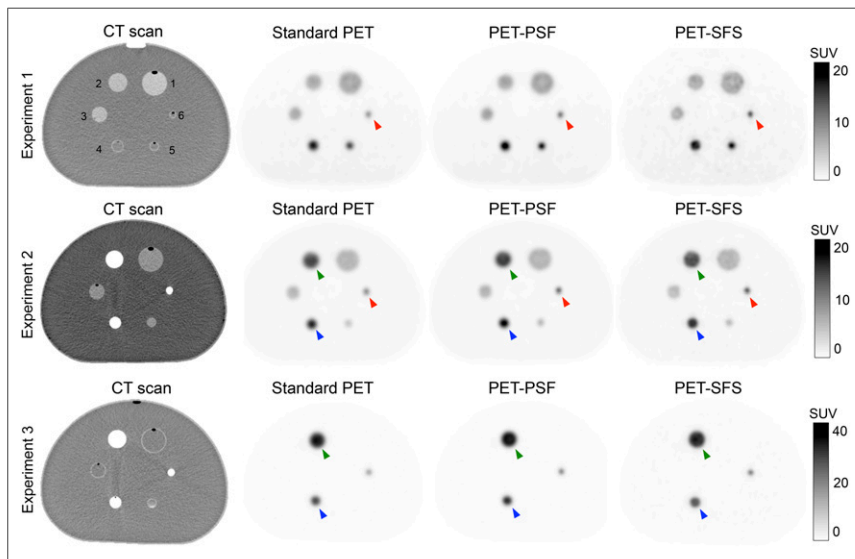

FIGURE 2. ^{18}F-fluoride PET/CT transaxial images of 3 different phantom experiment acquisitions (1 for each line). Alongside CT image (first column) are 3 different types of functional images: standard PET images (second column), images resulting from inclusion of PSF model into reconstruction (third column), and images resulting after application of SFS resolution recovery algorithm (fourth column). For detailed information on lesion volume, CM, and ^{18}F-FDG concentrations, refer to Table 1. Green markers highlight sphere 2, blue markers highlight sphere 4, and red markers highlight sphere 6.

with active skeletal metastases were included in the analysis, 4 with prostate cancer and 3 with breast cancer.

In each patient, a whole-body ^{18}F-fluoride PET/CT scan was acquired with a total of 8 bed positions, from the base of the skull to upper thighs, 60 min after injection of approximately 250 MBq.

The image reconstruction protocol for both datasets was the same as for the phantom experiment, with the exclusion of the PSF reconstruction, which was not performed as it was not included in the clinical protocol.

Data Analysis

In-house software was used to perform quantitative analysis on both phantom and patient data. An ROI was manually drawn on the outer border of each lesion to completely contain the whole lesion volume (or sphere for the phantom data) and then automatically segmented with a threshold of 40% of the maximum value of the ROI. The mean standardized uptake value (SUV$_{mean}$), maximum SUV (SUV$_{max}$), peak SUV (SUV$_{peak}$), and lesion metabolic active tumor volume (MATV) were then computed for the automatically segmented ROI. SUV$_{peak}$ is computed here as the SUV$_{mean}$ measured over a fixed small circular volume of about 1 cm^3, in the hottest area of the tumor (more active region). It is considered more reproducible because it involves the mean value of a few voxels involving and surrounding the hottest tumor area.

Solely for the phantom experiments, knowing the ground truth, we used the root mean square error (RMSE) and contrast-to-noise ratio (CNR) as additional metrics for image-quality assessment. Specifically, we evaluated the quantification accuracy and the trade-off between contrast improvement and image noise. The 2 metrics are defined as follow

$$RMSE = 100 \times \sqrt{\frac{(A_S - A_{S,true})^2}{A_{S,true}^2}}$$

$$CNR = \frac{A_S - A_{back}}{\sigma_{back}}$$

A_S represents the mean activity estimated inside a sphere and $A_{S,true}$ the corresponding ground truth whereas A_{back} is the mean activity estimated in the phantom background and σ_{back} its SD.

RESULTS

Phantom Data

Figure 2 shows representative transaxial views of structural (CT) and functional (PET) images for the 3 phantom experiments, 1 for each line. PET images from PSF reconstruction (PET-PSF) and from the application of the resolution recovery algorithm (PET-SFS) are also displayed. Supplemental Figure 2 shows representative line profiles for the 3 experiments for spheres 4–5.

Improved qualitative resolution for the smaller structures (red marker in Fig. 2) is noted when the SFS-RR algorithm is applied. Even though larger spheres (green and blue markers in Fig. 2) are easily detectable in the images from all modalities, it is possible to

TABLE 2
Quantitative Results of Phantom Experiments

Experiment	SUV$_{mean}$ (g/mL)			SUV$_{max}$ (g/mL)			SUV$_{peak}$ (g/mL)			Ground truth (g/mL)	MATV (cm^3)			
	PET	PET$_{PSF}$	PET$_{SFS}$	PET	PET$_{PSF}$	PET$_{SFS}$	PET	PET$_{PSF}$	PET$_{SFS}$		PET	PET$_{PSF}$	PET$_{SFS}$	Ground truth
1														
S1	5.66	5.95	6.44	8.45	8.84	10.03	8.03	8.17	8.19	9.60	32.22	30.81	30.44	26.52
S2	5.29	5.64	6.28	8.50	9.00	10.69	8.50	8.8	7.88	9.60	13.84	13.20	12.47	11.49
S3	4.54	5.01	5.73	7.73	8.58	9.37	7.73	7.87	7.97	9.60	7.46	6.72	6.75	5.57
S4	10.22	12.25	13.17	18.64	22.12	22.11	18.64	16.25	18.24	24.87	3.52	2.86	3.33	2.57
S5	7.72	9.51	12.60	14.82	18.55	23.56	14.81	10.91	13.75	24.87	1.98	1.56	1.37	1.15
S6	4.21	5.27	8.50	8.19	10.52	16.92	4.77	10.51	11.96	24.87	1.34	1.10	0.83	0.52
2														
S1	4.65	4.87	5.16	6.85	7.08	7.78	6.62	6.69	6.54	8.67	34.28	32.96	31.03	26.52
S2	10.40	11.11	11.55	16.28	16.83	17.16	15.63	15.87	14.92	24.38	14.06	13.54	13.52	11.49
S3	3.87	4.25	4.60	6.74	7.25	7.57	6.09	6.61	6.39	8.67	7.53	6.89	6.53	5.57
S4	9.93	11.42	12.40	17.57	20.21	19.76	13.95	15.90	17.20	24.38	3.35	3.03	3.20	2.57
S5	2.49	3.08	4.02	4.97	6.05	7.71	3.14	3.57	4.76	8.67	2.32	1.71	1.37	1.15
S6	4.56	6.16	8.57	8.79	11.76	16.14	5.02	7.60	10.03	24.38	1.39	0.98	0.86	0.52
3														
S2	24.59	25.95	26.63	38.11	38.01	37.90	37.20	36.82	34.87	40.61	13.52	13.42	13.59	11.49
S4	16.68	19.08	20.74	29.92	34.12	33.97	23.78	26.89	29.19	40.61	3.35	3.08	3.25	2.57
S6	7.36	9.78	13.61	13.77	18.33	25.52	8.02	14.08	19.15	40.61	1.25	0.90	0.79	0.52

SUV$_{mean}$, SUV$_{max}$, SUV$_{peak}$, and MATV estimates computed for phantom spheres after automated segmentation for all experiments 1–3. Values are reported for estimates obtained with 3 different modalities (standard PET, PET reconstructed with a PSF model, and PET corrected with SFS-RR algorithm) alongside corresponding ground truth values.
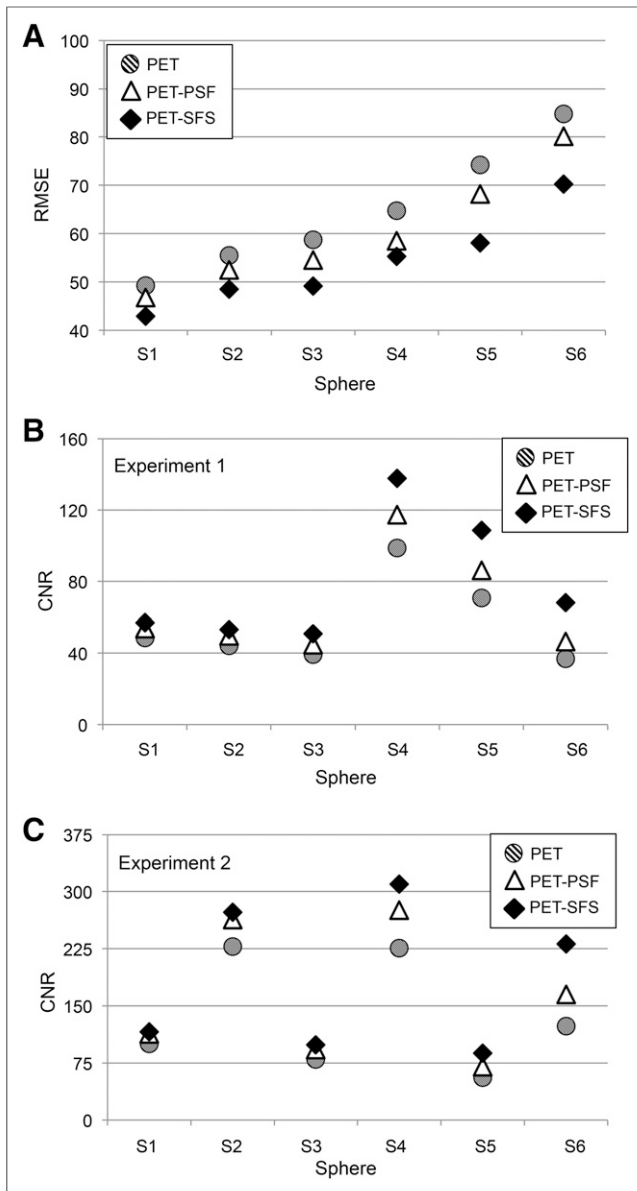
FIGURE 3. RMSE and noise analysis. For each sphere (S1–S6), 3 values corresponding to images obtained with different modalities are reported: standard PET (dashed circle), PET with PSF reconstruction (white triangle), and PET corrected with SFS-RR algorithm (black diamond). (A) RMSE for 6 spheres obtained as average among 3 phantom experiments. (B and C) CNR computed for each sphere against uniform region in phantom background. Only experiments 1 and 2 are reported for consistency reasons (in experiment 3, three spheres have zero activity).

appreciate a reduction in the blurring surrounding the structure when the resolution recovery algorithm is implemented.

Furthermore, it is possible to appreciate the robustness of the anatomy-based resolution recovery algorithm to unexpected mismatches between anatomy and functional acquisition by studying images from experiment 1. Even though spheres 4–6 cannot be detected on the CT image, they are not lost in the new functional image returned by the SFS-RR algorithm.

The quantitative evaluation of functional images obtained with the 3 different methods is reported in Table 2. The table reports for each phantom compartment in all the experiments the estimates of

SUV_{mean}, SUV_{max}, SUV_{peak}, and MATV together with the corresponding ground-truth values.

A summary of method performances is summarized in the supplemental materials (Supplemental Fig. 3) as the average among the 3 experiments. The general trend shows that the smaller the sphere, the bigger the bias in the activity estimation, regardless of the method used. However, with the SFS-RR application the bias decreases with an average range of 1%–5% in the PET-PSF images and 5%–19% in PET-SFS images. The same trend applies to lesion size estimation in which the bias decreases in a range of 0.46–0.95 cm for PET-PSF data and 0.56–1.09 cm for PET-SFS data.

The better performances of the SFS-RR algorithm are upheld by the RMSE and CNR comparison in Figure 3. Images resulting from the application of the SFS algorithm show lower RMSE on average (up to 15%, compared with standard PET for the smallest sphere) while being consistent with the trend of the RMSE increasing for smaller spheres. The improved image resolution does not come with reduced image quality because noise levels are contained with CNR either higher than or comparable with the standard PET image.

Clinical Dataset

The influence of using the SFS-RR algorithm on real patient data can be appreciated qualitatively in Figure 4 (and Supplemental Figs.
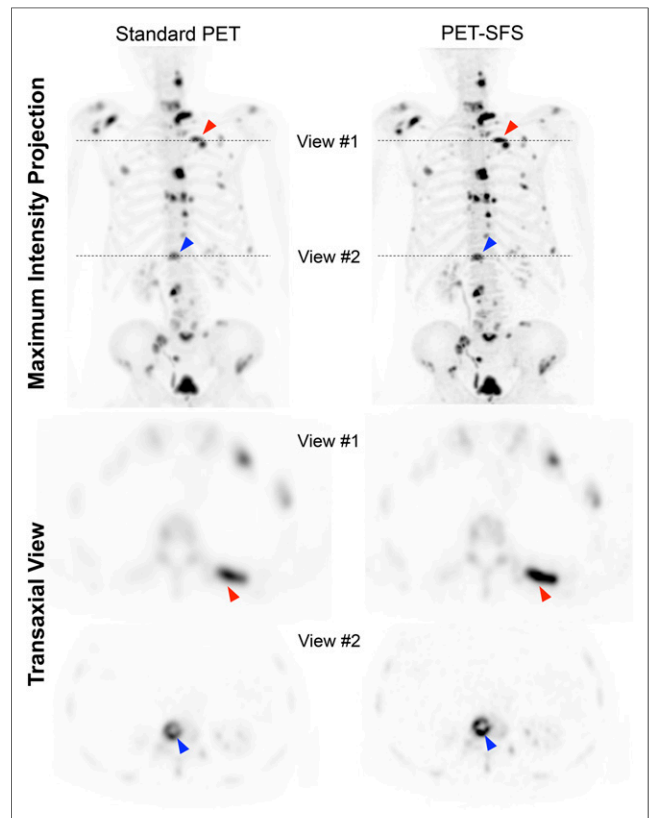

FIGURE 4. Maximum-intensity projection and transaxial views of representative subject (patient 01). (Left) Standard PET. (Right) PET corrected with SFS-RR algorithm. Red and blue markers highlight 2 representative lesions (spine and rib, respectively) that appear sharper in PET-SFS image than in standard PET 1. Dashed lines indicate slice position of transaxial views reported below maximum-intensity projection.

4–6) in which the maximum-intensity projection and 2 different transaxial views are displayed for a representative subject.

There is a clear increase in lesion sharpness after the application of a resolution recovery technique. The quantitative characterization of all lesions of this specific subject is reported in Supplemental Fig. 7 and Supplemental Table 1. The transaxial views of Figure 4 are a good example of the effect in lesion definition and characterization using the SFS-RR algorithm. Sharper contours and the activity recovery in the PET-SFS images for the rib lesion (Fig. 4, transaxial view, red marker) and also in the spine (Fig. 4, transaxial view, blue marker) are evident, and in the spine lesion it is easier to appreciate that the activity is in the periphery of the lesion in which there is greatest osteoblastic activity compared with the relatively photopenic center. In terms of quantitative characterization, there is an increase in the SUV_{mean} estimates of 60% (rib lesion, SUV PET = 30.7 and SUV SFS = 49.1) and 43% (spine lesion, SUV PET = 23.2 and SUV SFS = 33.1) from the standard PET to the PET-SFS. In contrast, the automatic segmented MATV has a relative reduction of 25% (rib lesion, MATV PET = 2.7 cm^3 and MATV SFS = 2.1 cm^3) and 31% (spine lesion, MATV PET = 7.5 cm^3 and MATV SFS = 5.2 cm^3).

A comprehensive comparison of the quantitative differences due to application of the SFS-RR algorithm is reported in Figure 5. As previously performed for patient 01 (Supplemental Fig. 7; Supplemental Table 1), we segmented all lesions of the remaining patients and collected the corresponding values of SUV_{mean}, SUV_{max}, SUV_{peak}, and MATV. Figure 5 reports the relative differences (SUVs and MATV) between lesions segmented in standard PET and PET-SFS images for the entire datasets.

There is a general increment in activity estimates for PET-SFS compared with standard PET. The average increments for different indices are as follow: ΔSUV_{mean} = 49%, ΔSUV_{max} = 47%, and ΔSUV_{peak} = 34%. For low-activity lesions, the range of differences in the estimates is larger than for more active lesions, indicating that the algorithm efficiency is dependent on signal-to-noise ratio. For the MATV, there is an average reduction of 1.4 cm^3 when segmentation is performed on PET-SFS images. When lesion size increased, the difference reached values of 4–5 cm^3, which might be relevant if patient classification were based on characterization of the larger detectable lesions.

DISCUSSION

In this work, we evaluated the influence of a multimodal PVC technique on the quantification and assessment of metastatic bone lesions from primary prostate and breast cancers. This work targets specifically to ^{18}F-fluoride PET/CT bone scanning because SFS-RR obviously produces better results when the correspondence between functional and structural signals is stronger. Our results showed an average 50% increase in SUV_{max} and SUV_{mean} and a 30% increase in the SUV_{peak} for partial-volume-corrected images when compared with the standard PET, depending on lesion size (lesion volume range, 0.5–25 cm^3). Our results are in agreement with findings in similar experimental settings from previous studies (31,32). Although SUV_{max} estimates depend on image noise, the 50% increase is not a consequence of noise bursts given the comparable RMSE between the SFS-RR–corrected images and standard PET images.

The higher activity recovery and the good noise control from the phantom analysis indicate a better image quality when the SFS-RR algorithm is applied. Indeed, patient images show lesions with sharper and better-defined contours, which result in improved lesion conspicuity and segmentation even for smaller volumes. The CNR depends on the absolute activity value, thus explaining why one set of spheres shows higher CNR than the other on Figure 3.

The results from the phantom experiments showed that the SFS-RR images outperform both standard PET and PSF images in terms of image quality and quantification accuracy. PSF-based image reconstruction is known to contribute to the appearance of artifacts (33) and is computationally cumbersome hence is not performed in routine clinical studies in our unit; for this reason, standard PET was used as a reference for SFS-RR images when it came to patient image analysis. In this regard, no artifacts have been generally observed in this and previous applications of SFS-RR, which is now a mature-enough technology worthy of further testing in the clinical setting.

It is worth highlighting the robustness of the methodology regarding possible mismatch between PET and CT images. Phantom acquisitions showed that even if some structures were visible only on the functional images, they were preserved after the application of the algorithm. This is of importance because lesions that might be lost in the CT segmentation, for example, due to their small size or the fact that the metastasis does not show sufficient bone mineralization to appear sclerotic, will still be visible in the final enhanced PET images.

Although the SFS-RR algorithm showed qualitatively and quantitatively better images than standard PET, further analyses are necessary to quantify the influence of the improved image quality on the assessment of patient skeletal staging and therapy response. Additional analyses may allow better definition and quantification of lesions after therapy or allow greater detectability and segmentation of metastatic spread at staging. Of additional interest would be the evaluation of whether lesion heterogeneity is affected by higher
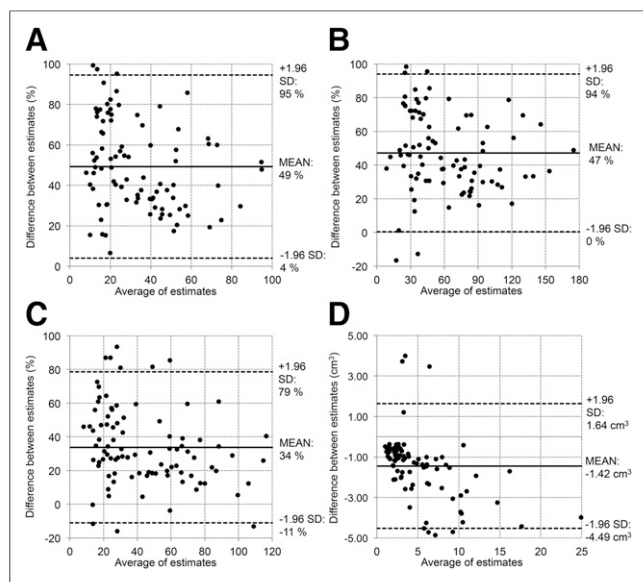

FIGURE 5. Bland–Altman plots showing differences in MATV and activity quantification when estimates are computed in images obtained with standard PET and PET corrected with SFS-RR algorithm. Each gray circle represents specific lesion; all lesions of all patients are reported. Differences between estimates for SUV_{mean} (A), SUV_{max} (B), and SUV_{peak} (C) are reported as relative percentage difference. MATV (D) is reported as absolute difference in cm^3.

resolution and evaluation of the consequent impact on textural analysis, given the increasing oncologic applications of textural analysis (*34,35*).

CONCLUSION

We have proposed and tested on a set of phantom studies and demonstrated on clinical data a multimodal methodology for quantitative resolution recovery for whole-body PET/CT, here specifically designed for ^{18}F-fluoride PET imaging of bone metastases. The technique allows rapid and straightforward application and produces images of significantly improved visual quality and quantitative properties.

REFERENCES

1. Rubens RD. Bone metastases: incidence and complications. In: Rubens RD, Mundy GR, eds. *Cancer and the Skeleton*. London, U.K.: Martin Dunitz; 2000:33–42.
2. Coleman RE, Rubens RD. The clinical course of bone metastases from breast cancer. *Br J Cancer*. 1987;55:61–66.
3. Clamp A, Danson S, Nguyen H, Cole D, Clemons M. Assessment of therapeutic response in patients with metastatic bone disease. *Lancet Oncol*. 2004;5:607–616.
4. Therasse P, Arbuck SG, Eisenhauer EA, et al. New guidelines to evaluate the response to treatment in solid tumors. *J Natl Cancer Inst*. 2000;92:205–216.
5. Scher HI, Halabi S, Tannock I, et al. Design and end points of clinical trials for patients with progressive prostate cancer and castrate levels of testosterone: recommendations of the Prostate Cancer Clinical Trials Working Group. *J Clin Oncol*. 2008;26:1148–1159.
6. Coleman RE, Mashiter G, Whitaker KB, Moss DW, Rubens RD, Fogelman I. Bone scan flare predicts successful systemic therapy for bone metastases. *J Nucl Med*. 1988;29:1354–1359.
7. Even-Sapir E, Metser U, Flusser G, et al. Assessment of malignant skeletal disease: initial experience with ^{18}F-fluoride PET/CT and comparison between ^{18}F-fluoride PET and ^{18}F-fluoride PET/CT. *J Nucl Med*. 2004;45:272–278.
8. Even-Sapir E, Metser U, Mishani E, Lievshitz G, Lerman H, Leibovitch I. The detection of bone metastases in patients with high-risk prostate cancer: ^{99m}Tc-MDP planar bone scintigraphy, single- and multi-field-of-view SPECT, ^{18}F-fluoride PET, and ^{18}F-fluoride PET/CT. *J Nucl Med*. 2006;47:287–297.
9. Galasko CSB. The pathological basis for skeletal scintigraphy. *J Bone Joint Surg Br*. 1975;57:353–359.
10. Ptáček J, Henzlová L, Koranda P. Bone SPECT image reconstruction using deconvolution and wavelet transformation: development, performance assessment and comparison in phantom and patient study with standard OSEM and resolution recovery algorithm. *Phys Med*. 2014;30:858–864.
11. Woodbury DH, Beierwaltes WH. Fluorine-18 uptake and localization in soft tissue deposits of osteogenic sarcoma in rat and man. *J Nucl Med*. 1967;8:646–651.
12. Beheshti M, Vali R, Waldenberger P, et al. The use of F-18 choline PET in the assessment of bone metastases in prostate cancer: correlation with morphological changes on CT. *Mol Imaging Biol*. 2009;11:446–454.
13. Young H, Baum R, Cremerius U, et al. Measurement of clinical and subclinical tumour response using [18 F]-fluorodeoxyglucose and positron emission tomography: review and 1999 EORTC recommendations. *Eur J Cancer*. 1999;35:1773–1782.
14. Stefano A, Gallivanone F, Messa C, Gilardi MC, Gastiglioni I. Metabolic impact of partial volume correction of [18F] FDG PET-CT oncological studies on the assessment of tumor response to treatment. *Q J Nucl Med Mol Imaging*. 2014;58:413–423.
15. Hatt M, Groheux D, Martineau A, et al. Comparison between ^{18}F-FDG PET image–derived indices for early prediction of response to neoadjuvant chemotherapy in breast cancer. *J Nucl Med*. 2013;54:341–349.
16. Soret M, Bacharach SL, Buvat I. Partial-volume effect in PET tumor imaging. *J Nucl Med*. 2007;48:932–945.
17. Rousset O, Rahmim A, Alavi A, Zaidi H. Partial volume correction strategies in PET. *PET Clin*. 2007;2:235–249.
18. Meltzer CC, Zubieta JK, Links JM, Brakeman P, Stumpf MJ, Frost JJ. MR-based correction of brain PET measurements for heterogeneous gray matter radioactivity distribution. *J Cereb Blood Flow Metab*. 1996;16:650–658.
19. Boussion N, Hatt M, Lamare F, Le Rest CC, Visvikis D. Contrast enhancement in emission tomography by way of synergistic PET/CT image combination. *Comput Methods Programs Biomed*. 2008;90:191–201.
20. Shidahara M, Tsoumpas C, Hammers A, et al. Functional and structural synergy for resolution recovery and partial volume correction in brain PET. *Neuroimage*. 2009;44:340–348.
21. Aston JAD, Cunningham VJ, Asselin M-C, Hammers A, Evans AC, Gunn RN. Positron emission tomography partial volume correction: estimation and algorithms. *J Cereb Blood Flow Metab*. 2002;22:1019–1034.
22. Rousset OG, Ma Y, Evans AC. Correction for partial volume effects in PET: principle and validation. *J Nucl Med*. 1998;39:904–911.
23. Qi J, Leahy RM, Cherry SR, Chatziioannou A, Farquhar TH. High-resolution 3D Bayesian image reconstruction using the microPET small-animal scanner. *Phys Med Biol*. 1998;43:1001–1013.
24. Rapisarda E, Bettinardi V, Thielemans K, Gilardi M. Image-based point spread function implementation in a fully 3D OSEM reconstruction algorithm for PET. *Phys Med Biol*. 2010;55:4131–4151.
25. Alessio AM, Stearns CW, Tong S, et al. Application and evaluation of a measured spatially variant system model for PET image reconstruction. *IEEE Trans Medical Imaging*. 2010;29:938–949.
26. Hammers A, Allom R, Koepp MJ, et al. Three-dimensional maximum probability atlas of the human brain, with particular reference to the temporal lobe. *Hum Brain Mapp*. 2003;19:224–247.
27. Turkheimer FE, Boussion N, Anderson AN, Pavese N, Piccini P, Visvikis D. PET image denoising using a synergistic multiresolution analysis of structural (MRI/CT) and functional datasets. *J Nucl Med*. 2008;49:657–666.
28. Molteni R. Prospects and challenges of rendering tissue density in Hounsfield units for cone beam computed tomography. *Oral Surg Oral Med Oral Pathol Oral Radiol*. 2013;116:105–119.
29. Kudo H, Nomura M, Asada T, Takeda T. Image processing method for analyzing cerebral blood-flow using SPECT and MRI. *IEEE Nucl Sci Symp Conf Rec*. 2007;5:4015–4021.
30. Grecchi E, O'Doherty J, Turkheimer FE. Exploiting anatomical information for PET image enhancement: a phantom experiment for algorithm validation. Paper presented at: IEEE Nuclear Science Symposium & Medical Imaging Conference; November 8–15, 2014; Seattle, WA.
31. Hatt M, Le Pogam A, Visvikis D, Pradier O, Le Rest CC. Impact of partial-volume effect correction on the predictive and prognostic value of baseline ^{18}F-FDG PET images in esophageal cancer. *J Nucl Med*. 2012;53:12–20.
32. Hoetjes NJ, van Velden FHP, Hoekstra OS, et al. Partial volume correction strategies for quantitative FDG PET in oncology. *Eur J Nucl Med Mol Imaging*. 2010;37:1679–1687.
33. Thielemans K, Asma E, Ahn S, et al. Impact of PSF modelling on the convergence rate and edge behaviour of EM images in PET. *IEEE Nucl Sci Symp Conf Rec*. 2010;3267–3272.
34. Cook GJ, Yip C, Siddique M, et al. Are pretreatment ^{18}F-FDG PET tumor texturalfFeatures in non–small cell lung cancer associated with response and survival after chemoradiotherapy? *J Nucl Med*. 2013;54:19–26.
35. Hatt M, Majdoub M, Vallieres M, et al. ^{18}F-FDG PET uptake characterization through texture analysis: investigating the complementary nature of heterogeneity and functional tumor volume in a multi–cancer site patient cohort. *J Nucl Med*. 2015;56:38–44.